BAYESIAN CALIBRATION OF A FINITE ELEMENT C-SPAR MODEL USING DIGITAL IMAGE CORRELATION

Carl Scarth[1*], Geir Olafsson[2], Janice M. Dulieu-Barton[2], Andrew T. Rhead[1] and Richard Butler[1]

[1] Materials and Structures Centre, Department of Mechanical Engineering, University of Bath, Claverton Down, Bath, BA2 7AY, UK

[2] Bristol Composites Institute, University of Bristol, Queen's Building, University Walk, Bristol, BS8 1TR, UK
* Corresponding author (c.scarth@bath.ac.uk)

Keywords: Model calibration, Data fusion, DIC, Finite Element Analysis, Uncertainty Quantification

ABSTRACT

Bayesian calibration is a statistical framework for combining data from experimental tests and numerical models, while formally accounting for uncertainty due to: i) unknown model inputs, ii) experimental observation errors, and iii) inaccuracies in the assumed model physics. Accurately quantifying such uncertainty can help ensure consistency when comparing Finite Element models with structural test data, and provide statistical confidence metrics in the predictions made by these models. This capability will be invaluable in enabling improved aircraft certification processes informed by virtual testing using combined data from mathematical models and component-level structural tests.

In this paper, Digital Image Correlation (DIC) data from preliminary compression tests of a composite C-spar are used to calibrate a Finite Element model of the spar, implemented in ABAQUS. Torsional springs are used to model the imperfectly clamped boundary conditions of the test specimen, which are considered uncertain. The aim of this study is to learn about the stiffness of these springs, as well as an uncertain longitudinal modulus and ply thickness. The primary contribution of this paper is to address challenges associated with calibrating the full-field nodal displacement output using the high-dimensional data produced by data-rich structural tests, in a efficient approach using Gaussian process emulators. Fitting the model to such a large volume of data is the key challenge addressed.

1 INTRODUCTION

Certification of composite aerospace structures is currently undertaken via a series of tests of increasing size and complexity known as a "test pyramid" or "building block" approach. Empirical knockdown factors based upon coupon test data are used along alongside relatively few tests at higher length-scales, leading to conservative strain limits, and reducing the benefits of tailoring in composite structures. Over-dependence on coupon tests may be overcome through virtual testing, combining data from both computer models and component-level experimental tests. To ensure consistency between these different sources of data, it is necessary to quantify the effects of myriad sources of uncertainty associated with unknown model inputs (e.g. defects/features [1], boundary conditions, variability in material properties [2]), experimental observation errors, and discrepancies [3] in model predictions due to incorrect or missing physics.

Uncertainty quantification using Finite Element (FE) models can be computationally expensive due to the large number of required model evaluations. It is therefore common to use nonparametric regression methods such as Gaussian Processes [4,5], Quantile Regression [6] or Kernel approaches [7] to create surrogates for FE models in uncertainty analyses. Gaussian Process Emulators are popular as these are highly versatile and can represent a large variety of complex functions, and can also give a pointwise estimate of uncertainty in predictions [4,5]. Gaussian processes have, for example, been used in stochastic finite element analysis [8], to model vibration of composite shells [9] and aeroelastic stability of composite plates [10] with uncertain properties, to predict failure of composite coupons subject to Open-Hole Tension [11], and in preliminary design of aircraft wings under uncertainty [12].

Bayesian model calibration [13,14] is a statistical framework for making predictions informed by both experimental and numerical data, while formally accounting for the above sources of uncertainty, and learning about parameters upon which both the mechanical model and physical system depend which cannot be controlled in experiments. The calibration framework proposed by Kennedy and O'Hagan [13] is built around Gaussian Process Emulators for efficiency, and explicitly incorporates uncertainty due to model discrepancy and observation error. When datasets are large this univariate approach can, however, result in a high-dimensional discretisation of the calibration problem which is extremely costly to solve, rendering it unsuitable for calibrating FE models using data rich full-field experimental techniques such as Digital Image Correlation (DIC). Higdon *et al*. [14] proposed a multivariate approach which uses Singular Value Decomposition (SVD) to obtain a reduced dimensional representation of simulation and experimental output to overcome this limitation. A similar approach was recently used by Ding *et al.* [15] to fit Gaussian Process Emulators to a full-field model output.

The aim of this paper is to demonstrate Bayesian model calibration by combining FE model output with data from structural tests of composite components. DIC displacement measurements from compression tests of a C-spar are used to calibrate an ABAQUS model of the spar. The multivariate calibration framework of [14] is used to fit an emulator, perform the calibration, and make subsequent predictions. In this preliminary investigation, modelling is limited to a fixed applied load in the linear regime. Calibration is used to learn about an imperfectly clamped boundary condition, the longitudinal modulus and ply thickness of the specimen. Comparisons between the calibrated model representing the "true" spar (with inputs inferred for the as-manufactured properties and actual test boundary condition), and experimental data are subsequently made using the calibrated model.

2 SPAR MANUFACTURE AND TESTING

Tests were performed on a C-spar with geometry taken from previous manufacturing trials [16,17], with key dimensions shown in Figure 1. The geometry incorporates a central recessed feature such as is commonly used to accommodate changes in thickness around pad-ups arising, for instance, where the pylon or landing gear attach to the wing box. The spar was manufactured from 24 plies of AS4/8552 unidirectional pre-preg with constant stacking sequence of $[(\pm 45)_3/(0/90)_3]_S$ across the spar, via Double Diaphragm Forming over a male mould at a temperature of 60°C, as outlined in [16].

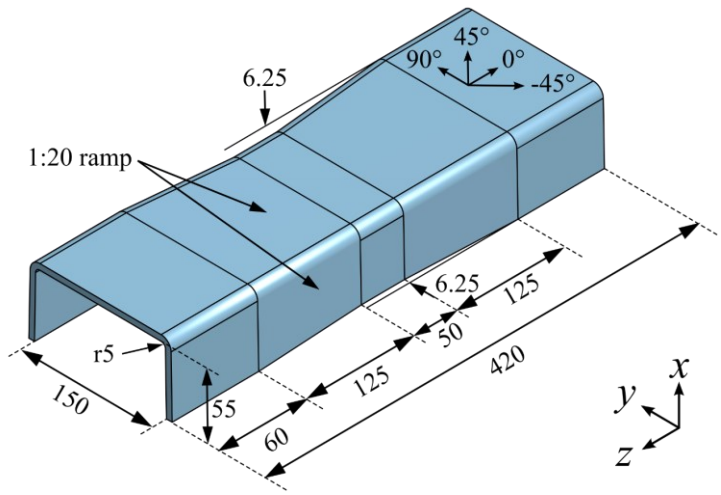

Figure 1: Geometry of C-spar. All dimensions are stated in mm, for the Inner Mould Line.

Preliminary quasi-static compression tests at an applied load of 10 kN have been undertaken at the University of Bristol. The spar was loaded about the end at z = 420 mm (see Figure 1). The ends of the spar were encapsulated in grooved steel blocks to prevent brooming to enforce a clamped boundary condition. The effective length between the blocks was 420 mm, with the spar trimmed to slightly longer

and the excess length embedded within the block grooves using a two-part epoxy resin (Araldite 2011). The block and spar assembly was mounted between flat platens so that the line of action of the load was through the centroid of the spar. Stereo DIC was carried out with two FLIR Blackfly 12 MP cameras with 100 mm Tokina lenses to track deformation of the spar surface during the test using the MatchID image acquisition and processing system [18]. Analysis is restricted to a field of view focussed on an external corner of the spar, capturing displacement in both the web and a single flange. The images were processed using Zero Normalised Sum of Squared Differences (ZNSSD) correlation, a step size of 10 and a subset size of 41, to produce a point cloud of 4117 measurements. Displacement components *u*, *v* and *w* were provided in a Cartesian coordinate system with x-axis aligned approximately with the spar longitudinal axis, misaligned with the model coordinate system shown in Figure 1.

3 FINITE ELEMENT MODEL

The C-spar is modelled in ABAQUS [19] using C3D8 hexahedral elements and an approximate element size of 5 mm, with a single element through the thickness of each ply, resulting in 116877 nodes. A static analysis is undertaken with geometric nonlinearity enabled. A concentrated load of 10 kN is applied to a reference point at the section centroid at z = 420 mm, and beam Multi Point Constraints (MPCs) are used to tie all nodes at this section to the reference point such that the undeformed shape is retained, thus distributing the load and replicating the end blocks. A similar strategy is used at the unloaded end (z = 0 mm). Slack in the bolts used to fasten the end block to the test fixture resulted in an imperfect clamped boundary in the test, with some rotation observed about the y axis. To represent this condition, a torsional spring with stiffness K is tied to the reference points at each end of the beam, and rotation about all other axes is fixed to zero. Values of K close to zero result in a simply supported boundary condition, whereas as K tends to infinity the boundary becomes clamped. The model is summarised in Figure 2, which also shows longitudinal displacement, w, for the described cases.

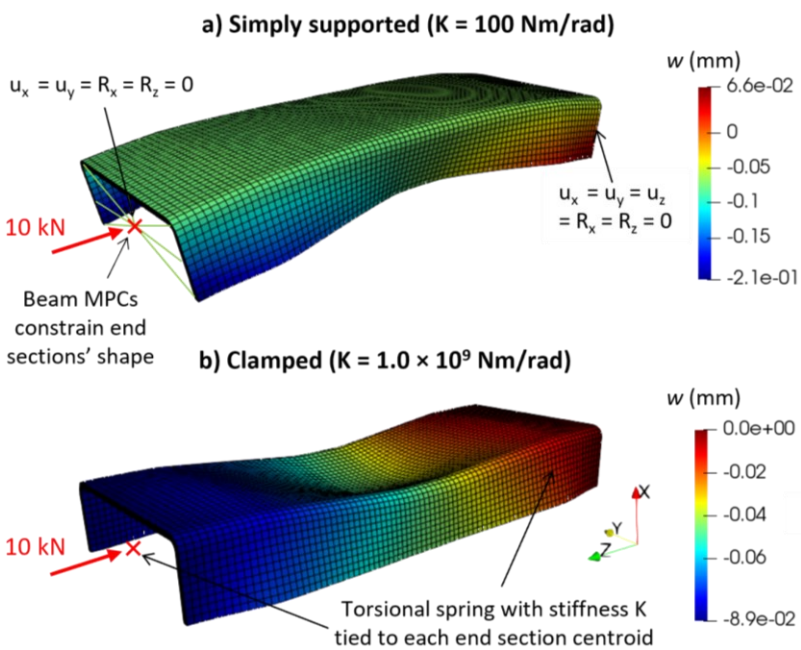

Figure 2: ABAQUS model boundary conditions and longitudinal displacement, *w,* plotted on (exaggerated) deformed shape for different torsional spring stiffnesses, *K*. Labelled boundary conditions apply to both cases, but are omitted for clarity.

4 ALIGNMENT OF THE DIC DATA AND MODEL

To make comparisons between the FE model and DIC data it is useful to evaluate the model at the

coordinates of the experimental data. The DIC data is first aligned with the external surface of the mesh using the fine registration capability of open-source 3D point cloud and mesh processing software CloudCompare [20]. The resulting rotation matrix is also used to express the displacements in the model coordinate system. To correct for rigid body motion and set the displacement of the fixed end to zero, the mean displacement from ten points close to the fixed end is subtracted from all data points. Each point is subsequently projected onto the surface of the element with the closest centroid, to determine a set of Cartesian coordinates directly on the mesh. Although the chosen element may not actually be that which is closest to the point in question, this element is taken as an initial guess in an iterative search.

The projected points are subsequently expressed in the local natural coordinate system used by ABAQUS to define displacements within an element, which is illustrated for a quadrilateral element in Figure 3. This system transforms an arbitrary quadrilateral in x, y, z onto a regular square with coordinates g and h defined on the interval [-1, 1]. The coordinates of a brick element incorporate a third component, r, also defined on [-1, 1], however, this coordinate is equal to 1 for all points on the outer surface of the spar, hence the system reduces to that of a quadratic element.

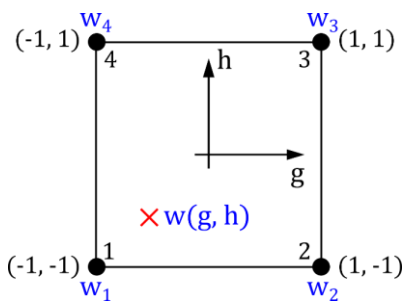

Figure 3: Natural coordinate system for a first order quadrilateral element [19]

To determine the longitudinal displacement at a specified set of natural coordinates $w(g,h)$, the displacement output at each of the four nodes, $w_{1\text{-}4}$, may be interpolated using [19]:

$$w(g,h) = (1-g)(1-h)\frac{w_1}{4} + (1+g)(1-h)\frac{w_2}{4} + (1+g)(1+h)\frac{w_3}{4} + (1-g)(1+h)\frac{w_4}{4} \quad (1)$$

The forward mapping from natural coordinates g and h to Cartesian coordinates is provided by substituting nodal coordinates x_i, y_i and z_i for w_i in Eq. (1), yielding a set of three equations. The inverse mapping from the Cartesian coordinates of the projected DIC data, onto their corresponding element natural coordinates, is provided by solving this set of equations. As there is no general closed-form solution for this mapping, a Newton-Raphson approach has been implemented as described in [21]. Convergence of the Newton-Raphson to g or h values outside of the interval [-1, 1] is taken as an indication that the initial choice of element is incorrect. As the FE mesh used in this paper forms a regular grid, the converged value of g and h is used to inform the direction of the search for the correct element. For example, if g converges to a value greater than 1, the above process is repeated for the adjacent element in the direction of increasing g, which is to the right in Figure 3. Points found to be outside of the domain of the finite element mesh are removed from the dataset.

For 4117 data points the described mapping converged in approximately 10 seconds. The aligned and projected DIC data points are overlaid on the model in Figure 4a). The subsequent mapping is illustrated in Figure 4b) by the plotting the data at their natural coordinates, within square elements defined on $g, h \in [-1, 1]$, arranged in a regular grid according to each element's position in the mesh.

5 BAYESIAN MODEL CALIBRATION

5.1 Case study overview

The aim of the calibration is to learn about the values of model uncertain model inputs which are representative of the underlying properties of the physical test. This case study will seek to learn about

`

the imperfectly clamped boundary condition described in Section 3, a significant source of uncertainty in the test, by learning about the stiffness, K, of the torsional springs used in the model. Values will also be inferred for the longitudinal modulus, E_{11}, and ply thickness, t_{ply}, as example material and geometric properties. These properties are uncertain as variability across pre-preg batches, albeit small, means that precise values are not known for the test specimen. For simplicity, this preliminary calibration case study will learn about these quantities based solely upon the longitudinal displacement, w.

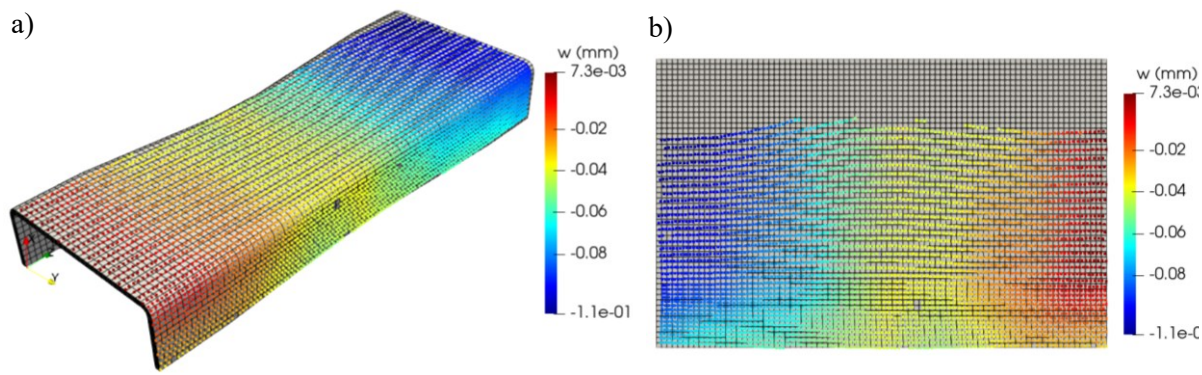

Figure 4: Alignment of the DIC data with the model: a) projection of data onto the model surface in Cartesian coordinates, and b) data expressed in natural coordinates of the corresponding element, arranged in a regular grid, with local coordinates of each element defined on $g, h \in [-1,1]$. Colour bars indicate longitudinal displacement, w.

Bayesian inference requires the specification of a prior distribution for all uncertain quantities, representing belief in their values before seeing the test data. A statistical model for the data must also be given, which dictates the likelihood function. Once these are specified, posterior samples may be drawn, representing belief in the values of the uncertain quantities after seeing the data. The selected statistical model is summarised in the following Subsections. Prior distributions for the uncertain inputs are summarised in Table 1. The prior on spring stiffness, K, is taken as log-uniform, with bounds chosen to span behaviour ranging from simply supported to clamped, as determined from a parametric study. The results of this study are shown in Figure 5, overlaid with the prior Probability Density Function (PDF). A log-uniform prior is chosen as the observed switch in response occurs over a log scale.

Input	Distribution	Parameter 1	Parameter 2
K (Nm/rad)	Log-uniform	100.0	1.0×10^9
E_{11} (GPa)	Gaussian	115.6	6.0
t_{ply} (mm)	Gaussian	0.196	5.0

Table 1: Prior distribution parameters for the uncertain model inputs. Parameters 1 and 2 are the mean and Coefficient of Variation (CoV, %) respectively for a Gaussian distribution, and the lower and upper bounds for log-uniform. Parameters for E_{11} are taken from published coupon test data [22]. The mean t_{ply} is taken from [23], with CoV chosen by engineering judgment.

5.2 Gaussian process emulator for high-dimensional model output

A simplified version of the multivariate framework from [14] is used to calibrate the FE model. This method is selected as both the model output and DIC data are high-dimensional, each comprised of thousands of entries. For computational efficiency, a Gaussian process emulator is used as a surrogate

model for the displacement. To render the Bayesian inverse problem tractable, the dimension of the data is reduced via an efficient decomposition into a p-dimensional basis representation of the displacement.

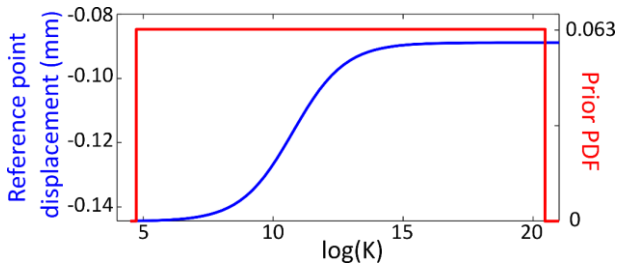

Figure 5: Parametric study showing longitudinal displacement, w, of the reference point at the loaded end of the spar against the natural logarithm of spring stiffness, K, with the prior PDF overlaid.

The p-dimensional basis representation of the model output may be expressed as

$$\boldsymbol{\eta}(\boldsymbol{\theta}) = \sum_{i=1}^{p} \boldsymbol{k}_i w_i(\boldsymbol{\theta}) + \boldsymbol{\epsilon} \tag{2}$$

where $\boldsymbol{\eta}(\boldsymbol{\theta})$ denotes the FE model output, a n_η-dimensional vector where n_η is the number of nodes, $\boldsymbol{\theta}$ is a d-dimensional vector of uncertain model inputs, $\boldsymbol{k}_1, \dots, \boldsymbol{k}_p$ are a set of n_η-dimensional orthogonal basis vectors, $w_i(\boldsymbol{\theta})$ are coefficients which capture dependence upon of the displacement upon the uncertain inputs, and $\boldsymbol{\epsilon}$ is the error induced by truncating the expansion. A surrogate model is constructed by fitting Gaussian process emulators to each w_i, across the space of uncertain inputs $\boldsymbol{\theta}$.

The emulators are trained using the model output for a set of m Latin Hypercube Samples of uncertain inputs, $\boldsymbol{\theta}_1^*, \dots, \boldsymbol{\theta}_m^*$. The longitudinal displacement predictions across all nodes of each sample are stored in vector $\boldsymbol{\eta}_i$, and standardised such that the mean nodal displacement is zero, and overall variance is one. The standardised samples are combined into matrix $\boldsymbol{\Xi} = [\boldsymbol{\eta}_1, \dots, \boldsymbol{\eta}_m]$, and basis vectors $\boldsymbol{k}_1, \dots, \boldsymbol{k}_p$ are obtained via SVD of $\boldsymbol{\Xi}$, retaining the first p terms. Following [24], the basis vectors are scaled such that each $w_i(\boldsymbol{\theta})$ may be modelled as a Gaussian process with zero mean and variance close to 1.

The ABAQUS model has been run for fifty samples, the outputs of which are used to create a set of four basis vectors, which are illustrated in Figure 5. These vectors represent the first four principal components of the longitudinal displacement across the training dataset. Truncating the expansion at $p = 4$ was found to explain the total variance of the training data within a tolerance of 10^{-4}%.

Each w_i From Eq. (2) is modelled as a zero-mean Gaussian process (GP), with prior distribution,

$$w_i \sim GP\left(0, \lambda_{wi}^{-1} R(\boldsymbol{\theta}, \boldsymbol{\theta}' | \boldsymbol{\rho}_i)\right) \tag{3}$$

where "$\sim$" denotes "is distributed as," λ_{wi} is the precision of the emulator of w_i, and $R(\boldsymbol{\theta}, \boldsymbol{\theta}' | \boldsymbol{\rho}_i)$ is a covariance function given as

$$R(\boldsymbol{\theta}, \boldsymbol{\theta}' | \boldsymbol{\rho}_i) = \prod_{j=1}^{d} \rho_{ij}^{4\left(\theta_j - \theta_j'\right)^2} \tag{4}$$

where $\boldsymbol{\theta}$ and $\boldsymbol{\theta}'$ are different realisations of input vector $\boldsymbol{\theta}$, and $\boldsymbol{\rho_i} = (\rho_{i1}, \dots, \rho_{id})$ is a vector of correlation length parameters for w_i, with component ρ_{ij} corresponding to the jth input θ_j.

Suppose that w_i is known for each of the m training data points and grouped together into a vector $\boldsymbol{w_i} = \left(w_i(\boldsymbol{\theta}_1), \dots, w_i(\boldsymbol{\theta}_m)\right)^T$, then all p of these vectors are combined into a mp-dimensional vector, $\boldsymbol{w} = \left(\boldsymbol{w}_1, \dots, \boldsymbol{w}_p\right)^T$. The prior distribution for $\boldsymbol{w}$ may be expressed as

$$\boldsymbol{w} \sim \mathcal{N}\left(\boldsymbol{0}_{mp}, \boldsymbol{\Sigma}_w\right) \tag{5}$$

$$\text{where,} \qquad \boldsymbol{\Sigma}_w = \text{diag}\left(\lambda_{wi}^{-1} R_{wi,\theta^*}, i = 1, \dots, p\right) \tag{6}$$

`

where $\mathcal{N}(\boldsymbol{\mu}, \boldsymbol{\Sigma})$ denotes a multivariate Gaussian distribution with mean $\boldsymbol{\mu}$ and covariance $\boldsymbol{\Sigma}$, and $R_{wi,\boldsymbol{\theta}^*}$ is the $m \times m$ matrix populated by applying Eq. (4) to every combination of training sample input values, with the entry in the jth row and k^{th} column given by $R(\boldsymbol{\theta}_j, \boldsymbol{\theta}_k | \boldsymbol{\rho}_i)$.

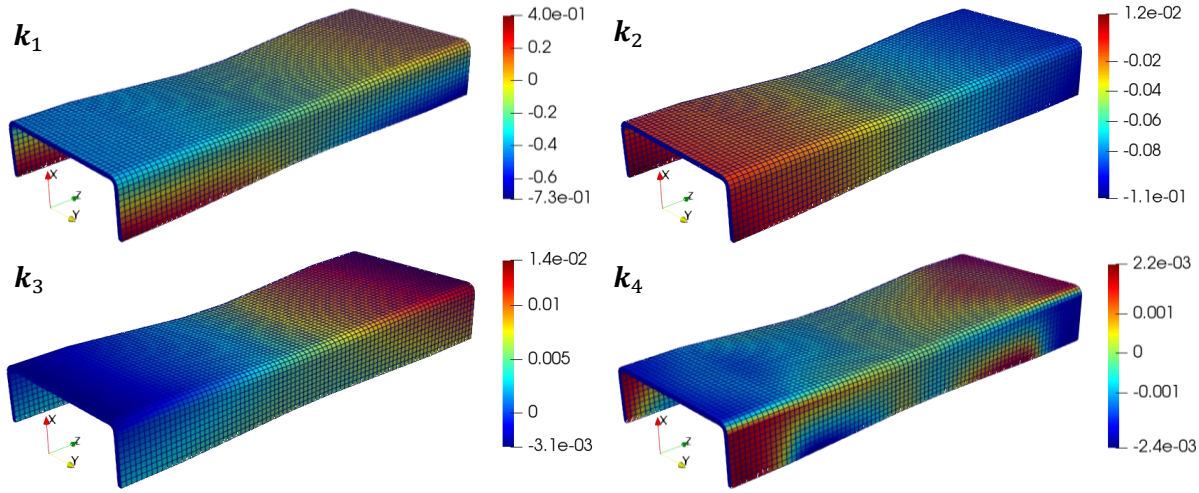

Figure 6: First four basis vectors computed using SVD of the ABAQUS longitudinal displacement output, w, for a set of 50 Latin Hypercube Samples.

5.3 Bayesian model calibration using high-dimensional data

The aim of calibration is to learn about a set of uncertain model inputs to match the conditions of the experiment. A simplified version of [14] is used, wherein all differences between the model and experimental data are attributed to a single error term, $\boldsymbol{e}$. If all DIC measurements of displacement, w, are grouped in a n_y-dimensional vector $\boldsymbol{y}$, the model for $\boldsymbol{y}$ may be stated as

$$\boldsymbol{y} = \boldsymbol{\eta}_y(\widehat{\boldsymbol{\theta}}) + \boldsymbol{e} \tag{7}$$

where $\boldsymbol{\eta}_{\mathrm{y}}(\widehat{\boldsymbol{\theta}})$ is the model output at the coordinates of the DIC data, with uncertain inputs set to $\widehat{\boldsymbol{\theta}}$, their "best" setting to match the conditions of the experiment. In Eq. (7), $\boldsymbol{\eta}_{\mathrm{y}}(\widehat{\boldsymbol{\theta}})$ is substituted with the series expansion and emulator described in Section 5.2. For compatibility, the data must be standardised in the same fashion as the model outputs using the training data mean and standard deviation. The mean vector must first be interpolated to the experimental data points, using Eq. (1) and the natural coordinates of the DIC data, determined as outlined in Section 4. Basis vectors $\boldsymbol{k}_{\mathrm{i}}$ must likewise be interpolated to give a set of n_y-dimensional vectors $\boldsymbol{k}_{yi}$. Using Eqs. (2) and (7), the joint model for the experimental data and emulator training data may subsequently be expressed as

$$\begin{pmatrix} \boldsymbol{y} \\ \boldsymbol{\eta} \end{pmatrix} = \begin{bmatrix} \boldsymbol{K}_y & \boldsymbol{0} \\ \boldsymbol{0} & \boldsymbol{K} \end{bmatrix} \begin{pmatrix} \boldsymbol{u}(\widehat{\boldsymbol{\theta}}) \\ \boldsymbol{w} \end{pmatrix} + \begin{pmatrix} \boldsymbol{e} \\ \boldsymbol{\epsilon} \end{pmatrix} \tag{8}$$

where $\boldsymbol{\eta} = (\boldsymbol{\eta}_1; \dots; \boldsymbol{\eta}_m)$ is the concatenation of model output for all training samples into a single vector, $\boldsymbol{K}_y$ is an $m \times n_y$ matrix of the interpolated basis vectors $[\boldsymbol{k}_{y1}, \dots, \boldsymbol{k}_{yp}]$, $\boldsymbol{K} = [\boldsymbol{I}_m \otimes \boldsymbol{k}_1, \dots, \boldsymbol{I}_m \otimes \boldsymbol{k}_p]$ where $\otimes$ is the Kronecker product and $\boldsymbol{I}_m$ is an $m \times m$ identity matrix, and $\boldsymbol{u}(\widehat{\boldsymbol{\theta}})$ is the p-dimensional representation of model at experimental input setting $\widehat{\boldsymbol{\theta}}$, with elements equivalent to $w_i(\widehat{\boldsymbol{\theta}})$ in Eq. (2). The reduced-dimensional experimental and model data has a joint prior given by

$$\begin{pmatrix} \boldsymbol{u}(\widehat{\boldsymbol{\theta}}) \\ \boldsymbol{w} \end{pmatrix} \sim \mathcal{N}\left(\boldsymbol{0}_{p(m+1)}, \boldsymbol{\Sigma}_z = \begin{bmatrix} \boldsymbol{\Sigma}_u & \boldsymbol{\Sigma}_{u,w} \\ \boldsymbol{\Sigma}_{u,w}^T & \boldsymbol{\Sigma}_w \end{bmatrix} \right) \tag{9}$$

where $\Sigma_u = \mathrm{diag}(\lambda_{w1}^{-1}, \dots, \lambda_{wp}^{-1})$, $\Sigma_{u,w} = \mathrm{diag}(\lambda_{wi}^{-1} R(\widehat{\boldsymbol{\theta}}, \boldsymbol{\theta}^* | \boldsymbol{\rho}_i), i = 1, \dots, p)$ and $R(\widehat{\boldsymbol{\theta}}, \boldsymbol{\theta}^* | \boldsymbol{\rho}_i)$ is a row vector populated using Eq. (4) to calculate the correlation of $\widehat{\boldsymbol{\theta}}$ with each training data point $\boldsymbol{\theta}_j$.

Calibration is an inverse problem; the quantities on the left-hand side of Eq. (8) are known, those on the right-hand side (the calibration inputs $\widehat{\boldsymbol{\theta}}$ and hyperparameters which govern the underlying Gaussian processes of $\boldsymbol{u}$ and $\boldsymbol{w}$ and error terms $\boldsymbol{e}$ and $\boldsymbol{\epsilon}$) are uncertain and must be given prior distributions. Priors for $\widehat{\boldsymbol{\theta}}$ are specified in Table 1. Following [14], $\beta(1.0, 0.1)$ priors are used for ρ_{ij} and $\Gamma(5.0, 5.0)$ for λ_{wi}. Components of $\boldsymbol{\epsilon}$ and $\boldsymbol{e}$ are taken as independent, identically distributed zero-mean Gaussian errors with precisions λ_η and λ_y having $\Gamma(a_\eta, b_\eta)$ and $\Gamma(a_y, b_y)$ priors. Parameters for λ_η are taken as a_η= 1.0 and b_η = 0.0001 [24]. Values of a_y = 5.0 and b_y = 0.05 are chosen to specify that the observation error is expected to be an order of magnitude smaller than the model output standard deviation.

Bayesian inference may be undertaken to sample from the posterior distribution of the uncertain quantities. Sampling using the full-field data, $\boldsymbol{y}$ and $\boldsymbol{\eta}$, is not tractable as each likelihood evaluation of the model specified by Eq. (8-9) requires the solution of $mn_\eta + n_y$ ($\approx 6 \times 10^6$) equations. An equivalent expression for the posterior is given by [14]:

$$\pi(\widehat{\boldsymbol{\theta}}, \boldsymbol{\lambda}_w, \boldsymbol{\rho}, \lambda_\eta, \lambda_y | \boldsymbol{y}, \boldsymbol{\eta}) \propto L(\hat{\boldsymbol{z}} | \widehat{\boldsymbol{\theta}}, \boldsymbol{\lambda}_w, \boldsymbol{\rho}, \lambda_\eta, \lambda_y)\pi(\widehat{\boldsymbol{\theta}})\pi(\boldsymbol{\lambda}_w)\pi(\boldsymbol{\rho})\pi(\lambda'_\eta)\pi(\lambda'_y) \tag{10}$$

where $\pi(\cdot)$ is a prior distribution, and the likelihood, $L(\hat{\boldsymbol{z}}|\cdot)$, is expressed as a function of vector, $\hat{\boldsymbol{z}} = \left(\left(\boldsymbol{K}_y^T\boldsymbol{K}_y\right)^{-1}\boldsymbol{K}_y^T\boldsymbol{y}; (\boldsymbol{K}^T\boldsymbol{K})^{-1}\boldsymbol{K}^T\boldsymbol{\eta}\right)$, the Ordinary Least Squares solution of Eq. (8). Each likelihood evaluation requires the solution of $p(m+1)$ equations (204 in this study). The prior for $\hat{\boldsymbol{z}}$ is given by

$$\hat{\boldsymbol{z}} \sim \mathcal{N}\left(\boldsymbol{0}, \boldsymbol{\Sigma}_z + \begin{bmatrix} \left(\lambda_y\boldsymbol{K}_y^T\boldsymbol{K}_y\right)^{-1} & \boldsymbol{0} \\ \boldsymbol{0} & \left(\lambda_\eta\boldsymbol{K}^T\boldsymbol{K}\right)^{-1} \end{bmatrix}\right) \tag{11}$$

and λ_η and λ_y are modified to λ'_η and λ'_y, with priors $\Gamma(a'_\eta, b'_\eta)$ and $\Gamma(a'_y, b'_y)$ respectively, where

$$a'_\eta = a_\eta + m(n_\eta - p)/2 \tag{12}$$

$$a'_y = a_y + (n_y - p)/2 \tag{13}$$

$$b'_\eta = b_\eta + \boldsymbol{\eta}^T(\boldsymbol{I} - \boldsymbol{K}(\boldsymbol{K}^T\boldsymbol{K})^{-1}\boldsymbol{K}^T)\boldsymbol{\eta}/2 \tag{14}$$

$$b'_y = b_y + \boldsymbol{y}^T\left(\boldsymbol{I} - \boldsymbol{K}_y\left(\boldsymbol{K}_y^T\boldsymbol{K}_y\right)^{-1}\boldsymbol{K}_y^T\right)\boldsymbol{y}/2 \tag{15}$$

Sampling from the posterior distribution described by Eq. (10) is undertaken via Hamiltonian Monte Carlo (HMC), using the No-U-Turn Sampler (NUTS) implemented in probabilistic programming language Stan [25]. It was found that modifying the prior on λ_y, as described in Eqs. (13) and (15), resulted in a very strong restriction on sampling causing convergence problems. To overcome this problem, a less restrictive prior model was selected which directly uses a_y and b_y in place of a'_y and b'_y. The method was further simplified by finding a Maximum A Posteriori (MAP) estimate for emulator hyperparameters $\boldsymbol{\rho}$, $\boldsymbol{\lambda}_w$ and λ_η by maximising the marginal posterior of $(\boldsymbol{K}^T\boldsymbol{K})^{-1}\boldsymbol{K}^T\boldsymbol{\eta}$, fixing these parameters to their optimised values, then sampling from the posterior in the remaining parameters.

5.4 Making calibrated predictions

Predictions of the displacement can be made using the calibrated model by sampling from the underlying Gaussian process, parametrised by the samples of the posterior distribution. Standard conditional Gaussian identities [4] are used to state the distribution of a new predictive sample of the reduced-dimensional output $\boldsymbol{w}^*(\widehat{\boldsymbol{\theta}}) = (w_1^*(\widehat{\boldsymbol{\theta}}), \dots, w_p^*(\widehat{\boldsymbol{\theta}}))$ at the sampled "best" setting of the calibration parameters $\widehat{\boldsymbol{\theta}}$, conditional upon the training data $\hat{\boldsymbol{z}}$. This distribution is given by

$$\boldsymbol{w}^*(\widehat{\boldsymbol{\theta}})|\hat{\boldsymbol{z}} \sim \mathcal{N}(\boldsymbol{\mu}_{w^*}, \boldsymbol{\Sigma}_{w^*}) \tag{16}$$

$$\text{where, } \boldsymbol{\mu}_{w^*} = \boldsymbol{\Sigma}_{\hat{z},w^*}^T\boldsymbol{\Sigma}_{\hat{z}}^{-1}\hat{\boldsymbol{z}}, \text{ and } \boldsymbol{\Sigma}_{w^*} = \boldsymbol{\Sigma}_u - \boldsymbol{\Sigma}_{\hat{z},w^*}^T\boldsymbol{\Sigma}_{\hat{z}}^{-1}\boldsymbol{\Sigma}_{\hat{z},w^*} \tag{17}$$

where $\boldsymbol{\Sigma}_{\hat{z},w^*} = [\boldsymbol{\Sigma}_u; \boldsymbol{\Sigma}_{u,w}^T]$ and all other terms are as defined previously. The predictions are transformed into displacements using the basis functions, $\boldsymbol{\eta}^*(\widehat{\boldsymbol{\theta}}) = \sum_{i=1}^p \boldsymbol{k}_i w_i^*(\widehat{\boldsymbol{\theta}})$. Note that the observation error is not included as the aim is to sample from the "true" response without experimental noise.

6 RESULTS AND DISCUSSION

The described method has been used to draw a set of 6000 posterior samples. A comparison of the marginal posterior PDFs of the calibration parameters against their prior distributions is shown in Figure 7. Scatter plots illustrating the prior and posterior correlation are shown in Figure 8.

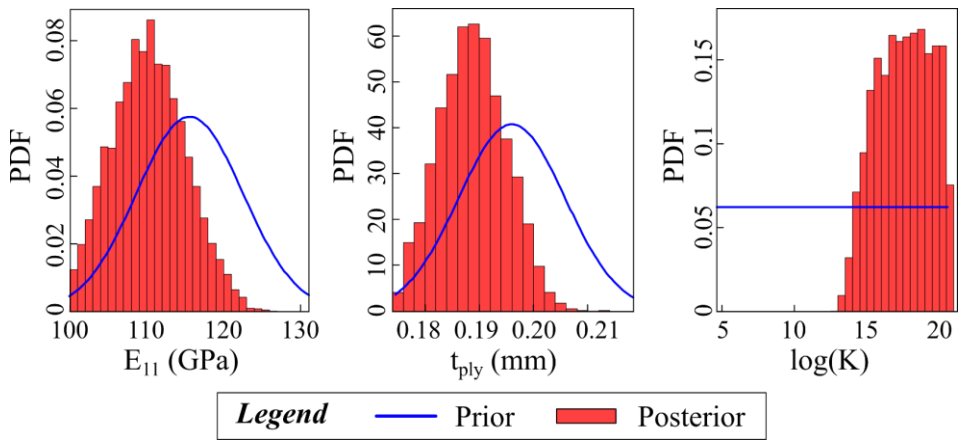

Figure 7: Comparison of Prior and Posterior distribution of the calibrated model inputs.

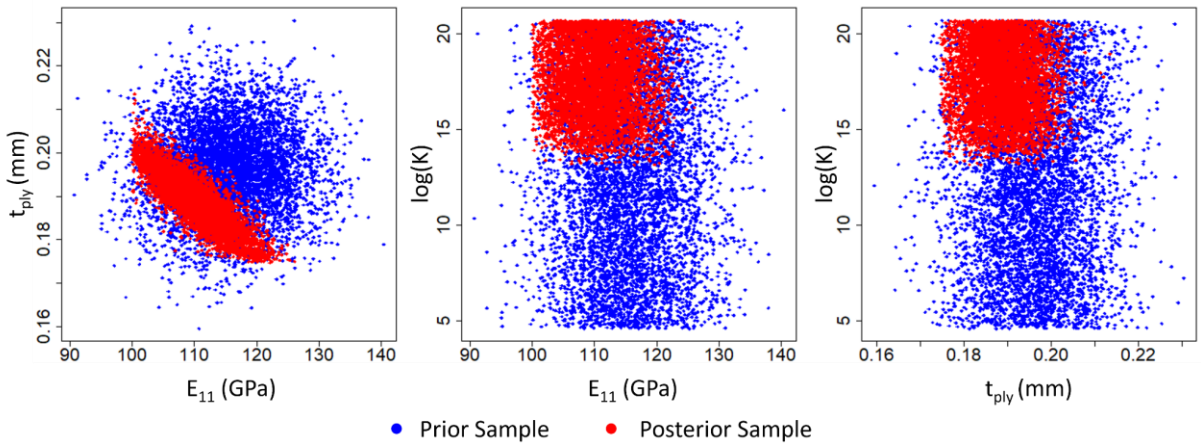

Figure 8: Scatter plots across the set of prior and posterior calibration input samples, illustrating posterior correlations.

The marginal distributions in Figure 7 show that uncertainty has been reduced in each calibration parameter, as each posterior distribution is narrower than the corresponding prior. This is the intended outcome of Bayesian inference, to reduce uncertainty by observing new data. Boundary condition spring stiffness, K, has most of the posterior mass at values with $\log(K) > 13$. Comparison with Figure 5 indicates that these values correspond mostly to a fully clamped boundary, with some allowance given to the possibility of imperfect clamping. The posterior distributions in E_{11} and the ply thickness are shifted to lower values, with modes 110.1 GPa and 0.188 mm respectively. The spar therefore likely had lower stiffness than would be predicted using nominal input values, and the uncalibrated model would likely under-predict the longitudinal displacement. A substantial reduction in uncertainty is also evident in Figure 8, wherein a strong negative correlation is observed between E_{11} and t_{ply}. This posterior correlation arises as the model outputs similar displacement for a lower thickness and a higher modulus, as a higher thickness and lower modulus, thus both possibilities could explain the experimental data.

Substituting the posterior samples through the predictive model described in Section 5.4 results in a set of sample longitudinal displacement predictions, each a possible "true" displacement field given the remaining uncertainty. This uncertainty can be integrated out of the formulation to produce a calibrated prediction by taking the mean across all sample predictions. The mean calibrated prediction and standard deviation, taken as a metric of uncertainty in the prediction, are shown in Figure 9. Calibrated predictions can be obtained at the coordinates of the DIC measurements using the interpolated basis vectors $\boldsymbol{k}_{yi}$, and point-by-point comparisons made with the DIC data. For example, the absolute value of the residual [26] given by subtracting the DIC displacement from calibrated predictions, $|\boldsymbol{\eta}_y^* - \boldsymbol{y}|$, may highlight regions of disparity between the two datasets. This metric is illustrated for the uncalibrated model with nominal input values, and calibrated model in Figure 10.

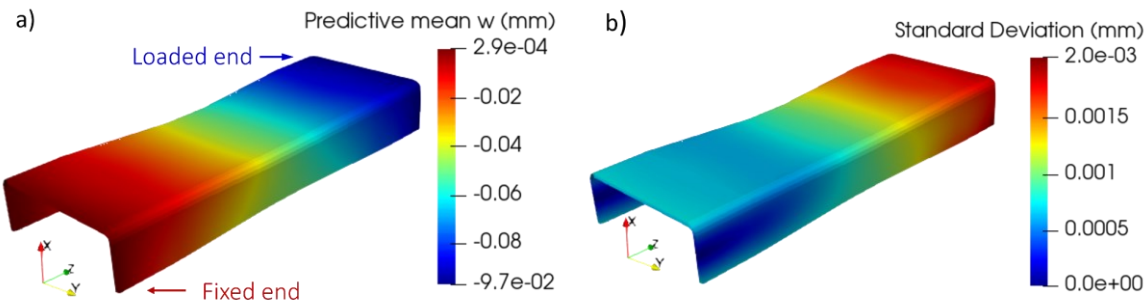

Figure 9: Calibrated predictive model of longitudinal displacement: a) mean prediction, and b) standard deviation of predictions.

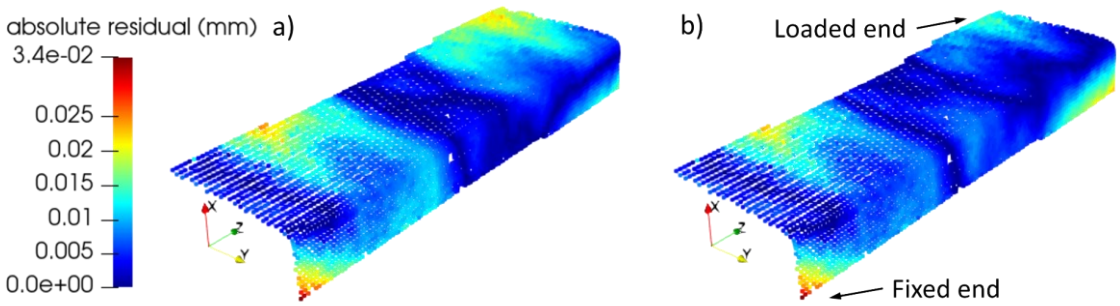

Figure 10: Plots of the absolute residual given by the difference between model and DIC data using: a) the uncalibrated model, and b) the calibrated model

The calibrated displacement in Figure 9a) resembles that of spar clamped at both ends, with a peak longitudinal displacement of -9.7×10^{-2} mm at the loaded end, resulting in an increase in magnitude from the nominal, uncalibrated value of -8.9×10^{-2} mm (see Figure 2) to match the higher experimental displacements (see Figure 4). This increase in displacement is achieved via the average reduction in axial stiffness and slight relaxation of the clamped boundary condition described above. The standard deviation in Figure 9b) shows a higher uncertainty in longitudinal displacement predictions at the loaded end than at the fixed end, which is an intuitive outcome. There is higher uncertainty in predictions at the tips of the flanges and in the webs relative to the centroid, due to the possibility of rotation arising at the ends in the test, but not being captured by the boundary conditions of the calibrated model.

Figure 10 shows lower residuals across more data points in the calibrated model compared with the nominal output, particularly near the loaded end of the web. The improvement is modest at this low applied load, although the extent of the shift in displacement is not fully evident due to the use of an

absolute error term and a change in sign of the residual across many points. Residuals relative to the calibrated model give a truer picture of discrepancies between the model and experiment, as they are less affected by input uncertainty. The highest disparities occur at the tip of the flange at both ends of the spar, possibly indicating that the torsional spring model inadequately captures the boundary condition. Fixing the *x* coordinates of the springs is one limitation of the chosen approach, and allowing the pivot location to vary as an uncertain input may improve the match with the data. Uncertainty in the zero experimental displacement, set as described in Section 4, also creates uncertainty in the *x* coordinate about which the spar can pivot. Large discrepancies are present towards the edge of the field of view in one ramp and in the furthest corner of the web, which are potentially due to observation error.

7 CONCLUSIONS

Bayesian model calibration has been applied to a Finite Element model of a C-spar loaded in compression, using DIC data. A calibration method has been implemented to overcome the challenges of using high-dimensional simulation and experimental data, while also being suitable for use with computationally expensive models. The procedure has been demonstrated in a simple case study using longitudinal displacement measurements around a corner of the spar, at fixed load of 10kN, to calibrate a model with uncertain longitudinal modulus, ply thickness, and boundary conditions. Uncertainty in each parameter was reduced following calibration, with posterior distributions shifted towards values resulting in lower axial stiffness and a slightly relaxed clamped boundary condition. A modest reduction was achieved in the absolute value of the residuals between the data and calibrated prediction.

Future work will aim to extend this method to a full test history across multiple fields of view. Calibration will be extended to all displacement components *u*, *v* and *w*, considering a broader range of uncertainties. Incorporating nonlinear behaviour and failure will warrant more complex models with a larger number of inputs, thus yielding further opportunities for improved learning.

ACKNOWLEDGEMENTS

The research presented was supported by the EPSRC Programme Grant 'Certification for Design – Reshaping the Testing Pyramid' (CerTest, EP/S017038/1). This support is gratefully acknowledged.

REFERENCES

[1] K. Potter, B. Khan, M. Wisnom, T. Bell, J. Stevens. Variability, fibre waviness and misalignment in the determination of the properties of composite materials and structures. *Compos Part A Appl Sci Manuf*, **39**, 2008, pp. 1343–54. doi:10.1016/j.compositesa.2008.04.016.

[2] S. Sriramula, M.K. Chryssanthopoulos. Quantification of uncertainty modelling in stochastic analysis of FRP composites. *Compos Part A Appl Sci Manuf,* **40**, 2009, pp. 1673–84. doi:10.1016/j.compositesa.2009.08.020.

[3] J. Brynjarsdóttir, A. O'Hagan. Learning about physical parameters: the importance of model discrepancy. *Inverse Probl*. **30**, 2014, 114007. doi:10.1088/0266-5611/30/11/114007.

[4] C.E. Rasmussen, C.K. Williams. *Gaussian Processes for Machine Learning*, MIT Press, 2006.

[5] J.E. Oakley, A. O'Hagan. Bayesian inference for the uncertainty distribution of computer model outputs. *Biometrika,* **89**, 2002, pp. 769–84. doi:10.1093/biomet/89.4.769.

[6] C. Davino, M. Furno, D. Vistocco. *Quantile regression: theory and applications*. John Wiley & Sons, 2013.

[7] B. Schölkopf, A.J. Smola, F. Bach. *Learning with kernels: support vector machines, regularization, optimization, and beyond*. MIT press, 2002.

[8] F.A. DiazDelaO, S. Adhikari. Gaussian process emulators for the stochastic finite element method. *Int J Numer Methods Eng,* **87,** 2011, pp. 521–40. doi:10.1002/nme.3116.

[9] S. Dey, T. Mukhopadhyay, S. Adhikari. Stochastic free vibration analyses of composite shallow doubly curved shells - a Kriging model approach. *Compos Part B Eng*, **70**, 2015, pp. 99–112. doi:10.1016/j.compositesb.2014.10.043.

[10] C. Scarth, P.N. Sartor, J.E. Cooper, P.M. Weaver, G.H.C. Silva. Robust and reliability-based aeroelastic design of composite plate wings. *AIAA J*, **55**, 2017, pp. 3539-3552.

doi:10.2514/1.J055829.

[11] T.R.C. Chuaqui, A.T. Rhead, R. Butler, C. Scarth. A data-driven Bayesian optimisation framework for the design and stacking sequence selection of increased notched strength laminates. *Compos Part B Eng.* **226**, 2021, 109347. doi: 10.1016/j.compositesb.2021.109347.

[12] R.M. Paiva, C. Crawford, A. Suleman. Robust and reliability-based design optimization framework for wing design. *AIAA J.* **52**, 2014, pp. 711–24. doi:10.2514/1.J052161.

[13] M.C. Kennedy, A. O'Hagan. Bayesian calibration of computer models. *J R Stat Soc Ser B Statistical Methodol.* **63**, 2001, pp. 425–64. doi:10.1111/1467-9868.00294.

[14] D. Higdon, J. Gattiker, B. Williams, M. Rightley. Computer model calibration using high-dimensional output. *J Am Stat Assoc* 2008;103:570–83. doi:10.1198/016214507000000888.

[15] C. Ding, H. Rappel, T. Dodwell. Full-field order-reduced Gaussian Process emulators for nonlinear probabilistic mechanics. *Comput Methods Appl Mech Eng*, **405**, 2023, 115855. doi:10.1016/j.cma.2022.115855.

[16] K.J. Johnson, R. Butler, E.G. Loukaides, C. Scarth, A.T. Rhead. Stacking sequence selection for defect-free forming of uni-directional ply laminates. *Compos Sci Technol*, **171**, 2019, pp. 34-43. doi:10.1016/j.compscitech.2018.11.048.

[17] C. Scarth, Y. Chen, C. Aza, A.T. Rhead, R. Butler. Manufacture of long spars: Laminate design, experimental trials and non-destructive evaluation. *Compos Part B Eng*. **255,** 2023, 110646. doi:10.1016/j.compositesb.2023.110646.

[18] MatchID, http://www.matchid.eu, accessed 15 May 2023.

[19] Abaqus Analysis User's Guide, Version 6.14. Dassault Systèmes, Simulia Corp, Providence, RI, USA, 2014.

[20] CloudComapare Version 2.11.3 [GPL Software], https://www.cloudcompare.org/, 2023.

[21] E.R. Denlinger, J. Irwin, P. Michaleris. Thermomechanical modeling of additive manufacturing large parts. *J Manuf Sci Eng,* **136***,* 2014. doi:10.1115/1.4028669.

[22] E. Clarkson. Hexcel 8552 AS4 unidirectional prepreg qualification statistical analysis report: FAA special project number SP4614WI-Q. Wichita, Kansas, 2011.

[23] L.E. Culliford, C. Scarth, T. Maierhofer, R. Jagpal, A.T. Rhead, R. Butler. Discrete stiffness tailoring: optimised design and testing of minimum mass stiffened panels. *Compos Part B Eng*. **221**, 2021, 109026. doi:10.1016/j.compositesb.2021.109026.

[24] S. Habib, K. Heitmann, D. Higdon, C. Nakhleh, B. Williams. Cosmic calibration: constraints from the matter power spectrum and the cosmic microwave background. *Phys Rev D.* **76**, 2007, 83503. doi:10.1103/PhysRevD.76.083503

[25] Stan Development Team. Stan modeling language users guide and reference manual, Version 2.26.1, https://mc-stan.org, 2023.

[26] J.S. Callaghan, D. Crump, A.S. Nielsen, O.T. Thomsen, J.M Dulieu-Barton. Quantitative full-field data fusion for evaluation of complex structures, *Exp Mech.*, 2023 (accepted subject to minor revision).

`